Available online at www.sciencedirect.com
ScienceDirect
Trans. Nonferrous Met. Soc. China 28(2018) 1007−1015
Transactions of Nonferrous Metals Society of China
www.tnmsc.cn

Numerical simulation for macrosegregation in direct-chill casting of 2024 aluminum alloy with an extended continuum mixture model

Hai-jun LUO[1], Wan-qi JIE[1], Zhi-ming GAO[1], Yong-jian ZHENG[2]

1. State Key Laboratory of Solidification Processing, Northwestern Polytechnical University, Xi'an 710072, China;
2. Chair of Simulation and Modeling of Metallurgical Processes, Montan Universitaet Leoben, 8700 Leoben, Austria

Received 22 June 2017; accepted 24 April 2018

Abstract: An extended continuum mixture model for macrosegregation is applied to predicting Cu and Mg segregation in large-size ingot of 2024 aluminum alloy during direct chill casting (DC). A microsegregation model using the approximate phase diagram data was coupled with macroscopic transport equations for macrosegregation profiles. Then, the impacts of transport mechanisms on the formation of macrosegregation were discussed. It is found that copper and magnesium have a similar segregation configuration from the billet center to surface. Negative segregation is observed in the centerline and subsurface, whereas positive segregation is obtained in the surface and somewhat underestimated positive segregation in the middle radius. Further, the discrepancy between the predicted and experimental results was discussed in detail. The results show that the magnesium to some extent alleviates the copper segregation in ternary alloy, compared with that in binary alloy. The predicted results show good agreement with measured experimental data obtained from literatures.

Key words: direct-chill casting; macrosegregation; numerical simulation; continuum model; 2024 aluminum alloy

1 Introduction

Direct chill (DC) casting is a semi-continuous process, which has been widely used for the production of extrusion billets and rolling ingots of aluminum alloys. The technological details of DC casting can be found in literatures [1−3]. Macrosegregation, i.e. constitution variation in macro-scale, is a stubborn problem in this process, which destroys the homogeneity of the production in both microstructures and mechanical properties. This large scale non-uniform chemical composition cannot be eliminated by the following heat treatments. Therefore, it is of vital importance to depress the formation of macro-segregation during casting process.

The formation of macrosegregation depends mainly on the solute transport induced by thermosolutal convection, solidification shrinkage and molten metal injection during casting process. The settlement of the free-floating dendrites also contributes to the macrosegregation. The optimization of the process to reduce macrosegregation can be realized based on a well understanding of the transportation details during solidification, which can be quantitatively simulated by numerical method.

Modeling for macrosegregation in castings has been extensively investigated over the past half century [4−7]. To model the transport phenomena in DC casting, REDDY and BECKERMANN [8] studied the effects of mushy permeability, thermosolutal convection and solidification contraction on the macrosegregation pattern in DC casting of an Al−4.5%Cu (mass fraction) round ingot. They concluded that centerline segregation could be either positive or negative, depending upon the grain density and permeability of the mushy zone. VREEMAN et al [9,10] developed a mixture model for DC casting process with the consideration of free-floating dendrites and applied the model for Al−4.5%Cu and Al−6.0%Mg (mass fraction) binary alloys. The predicted surface-to-centerline distribution of macrosegregation was consistent with the patterns observed in DC ingots. Furthermore, they discussed the validity of model parameters and simulated the effect of

Foundation item: Project (51420105005) supported by the Major International (Regional) Joint Research Program of National Natural Science Foundation of China; Project (2016YFF0101301) supported by the National Key Research and Development Program of China
Corresponding author: Wan-qi JIE; Tel/Fax: +86-29-88495414; E-mail: jwq@nwpu.edu.cn
DOI: 10.1016/S1003-6326(18)64738-7

grain refiner on macrosegregation and fluid flow [11]. KRANE et al [12−14] proposed a thermodynamic closure continuum mixture model for ternary systems (Pb−Sb−Sn alloy) using an idealized ternary equilibrium phase diagram. Their results indicated that macrosegregation of the solutes was significantly different from that of binary systems. DU et al [15] studied the macrosegregation of a ternary Al−Cu−Mg alloy using a modified mapping technique to describe solidification paths [16]. The semi-quantitative results showed that the contribution of each solute element to the solutal buoyancy affected the final segregation pattern. Recently, VUŠANOVIĆ [17] applied a non-equilibrium microsegregation model in a horizontal DC casting ternary Al−4.5%Cu−1.0%Mg (mass fraction) alloy. They found that the copper exhibited less segregation compared to Al−Cu alloy, while magnesium had a similar segregation profile but less pronounced. ELLINGSEN et al [18,19] modeled macrosegregation in a 5182 aluminium alloy accounting for secondary phase formation. A more detailed review of macrosegregation modelling was given in Ref. [20].

In the present work, we extended the continuum mixture model of VREEMAN and coworkers [11] to the multi-component system and used Scheil equation instead of equilibrium assumption. The new method was used to calculate the macrosegregation on industrial large-scale DC ingots of 2024 aluminum alloy, with a diameter of 400 mm and length of 950 mm. Three alloying elements, Cu, Mg and Mn, are included. The solidification path in the 2024 alloy is complex for elements more than three [1]. Since the partition coefficient of manganese is approximately 1, the segregation of manganese is ignored, and the alloy is reasonably reduced to a ternary system with the composition of Al−4.5%Cu−1.5%Mg (mass fraction). The calculation results were compared with the experimental data of DORWARD and BEERNTSEN [21] to prove the validation of our method.

2 Mathematical model

2.1 Macroscopic transport governing equations

Based on the continuum mixture model with free floating solid particles formulated by VREEMAN et al [9], separate and distinct mixture momentum equations are employed to calculate momentum transfer in two-phase regions (using Eqs. (2) and (4) in slurry region and Eqs. (3) and (5) in mushy zone). The macroscopic transport equations for heat, mass, momentum and species are described below, in which the following assumptions are adopted:

1) The fluid is incompressible, laminar and Newtonian flow regarding the inlet velocity in DC casting condition.

2) The solid−liquid regions consist of a slurry region of free floating solid particles and the mushy zone (divided by the packing solid fraction), which is considered to be a rigid and dendritic matrix saturated with interdendritic liquid. The primary phase and the secondary phases are treated as a single solid phase, which have the same physical properties.

3) Local equilibrium is assumed at the solid−liquid interface under DC casting.

4) The solute diffusion in liquid is infinite and neglected in the solid.

5) Boussinesq approximation is used to calculate the thermal and solute buoyancy.

The basic conservation equations are as follows.

Continuity equation:

$$\frac{\partial \rho}{\partial t}+\nabla\cdot(\rho \boldsymbol{V})=0 \tag{1}$$

Momentum in x direction:

$$\begin{aligned}\frac{\partial}{\partial t}(\rho u)+\nabla\cdot(\rho \boldsymbol{V} u)=&\nabla\cdot(u_{\mathrm{l}}\frac{\rho}{\rho_{\mathrm{l}}}\nabla u)-\nabla\cdot(u_{\mathrm{l}}\frac{\rho f_{\mathrm{s}}}{\rho_{\mathrm{l}}}\nabla u_{\mathrm{s}})+\\ &\nabla\cdot(\overline{u}_{\mathrm{s}}g_{\mathrm{s}}\nabla u_{\mathrm{s}})-\nabla\cdot[(\frac{\rho f_{\mathrm{s}}}{f_{\mathrm{l}}})(\boldsymbol{V}-\boldsymbol{V}_{\mathrm{s}})(u-u_{\mathrm{s}})]+\\ &g_{\mathrm{s}}(\rho_{\mathrm{s}}-\rho_{\mathrm{l}})\boldsymbol{g}-g_{\mathrm{s}}\rho_{\mathrm{s}}\boldsymbol{g}[\beta_{T,\mathrm{s}}(T-T_0)+\\ &\sum_{i=\mathrm{Cu,Mg}}\beta^i_{c,\mathrm{s}}(c^i_{\mathrm{s}}-c^i_0)]-g_{\mathrm{l}}\rho_{\mathrm{l}}\boldsymbol{g}[\beta_{T,\mathrm{l}}(T-T_0)+\\ &\sum_{i=\mathrm{Cu,Mg}}\beta^i_{c,\mathrm{l}}(c^i_{\mathrm{l}}-c^i_0)]-\frac{\partial P}{\partial x}\end{aligned} \tag{2}$$

$$\begin{aligned}\frac{\partial(\rho u)}{\partial t}+\nabla\cdot(\rho \boldsymbol{V} u)=&-\frac{\partial P}{\partial x}+\nabla\cdot(\mu\frac{\rho}{\rho_{\mathrm{l}}}\nabla u)-\\ &\frac{\mu_{\mathrm{l}}}{K}\frac{\rho}{\rho_{\mathrm{l}}}(u-u_{\mathrm{s}})+\rho_{\mathrm{l}}\boldsymbol{g}[\beta_{T,\mathrm{l}}(T-T_0)+\\ &\sum_{i=\mathrm{Cu,Mg}}\beta^i_{c,\mathrm{l}}(c^i_{\mathrm{l}}-c^i_0)]\end{aligned} \tag{3}$$

Momentum in r direction:

$$\begin{aligned}\frac{\partial(\rho v)}{\partial t}+\nabla\cdot(\rho \boldsymbol{V} v)=&\nabla\cdot(\mu_{\mathrm{l}}\frac{\rho}{\rho_{\mathrm{l}}}\nabla v)-\mu_{\mathrm{l}}\frac{\rho}{\rho_{\mathrm{l}}}\frac{v}{r^2}-\\ &\nabla\cdot(\mu_{\mathrm{l}}\frac{\rho f_{\mathrm{s}}}{\rho_{\mathrm{l}}}\nabla v)+\mu_{\mathrm{l}}\frac{\rho f_{\mathrm{s}}}{\rho_{\mathrm{l}}}\frac{v}{r^2}+\\ &\nabla\cdot(\overline{\mu}_{\mathrm{s}}g_{\mathrm{s}}\nabla v)-\overline{\mu}_{\mathrm{s}}g_{\mathrm{s}}\frac{v}{r^2}-\frac{\partial P}{\partial r}\end{aligned} \tag{4}$$

$$\begin{aligned}\frac{\partial(\rho v)}{\partial t}+\nabla\cdot(\rho \boldsymbol{V} v)=&-\frac{\partial P}{\partial r}+\nabla\cdot(\mu_{\mathrm{l}}\frac{\rho}{\rho_{\mathrm{l}}}\nabla v)-\\ &\frac{\mu_{\mathrm{l}}}{K}\frac{\rho}{\rho_{\mathrm{l}}}v+\mu_{\mathrm{l}}\frac{\rho}{\rho_{\mathrm{l}}}\frac{v}{r^2}\end{aligned} \tag{5}$$

Energy balance equation:

$$\frac{\partial(\rho H)}{\partial t}+\nabla\cdot(\rho H\boldsymbol{V})=\nabla\cdot(k\nabla T)-\nabla\cdot[\rho(H_1-H)(\boldsymbol{V}-\boldsymbol{V}_s)] \quad (6)$$

Diffusion equations for species Mg and Cu:

$$\frac{\partial(\rho c^{Cu})}{\partial t}+\nabla\cdot(\rho\boldsymbol{V}c^{Cu})=-\nabla\cdot(\rho f_l D_l\nabla c^{Cu})+$$
$$\nabla\cdot[(\rho f_l D_l\nabla(c_l^{Cu}-c^{Cu})]-$$
$$\nabla\cdot[\rho(c_l^{Cu}-c^{Cu})(\boldsymbol{V}-\boldsymbol{V}_s)] \quad (7)$$

$$\frac{\partial(\rho c^{Mg})}{\partial t}+\nabla\cdot(\rho\boldsymbol{V}c^{Mg})=-\nabla\cdot(\rho f_l D_l\nabla c^{Mg})+$$
$$\nabla\cdot[(\rho f_l D_l\nabla(c_l^{Mg}-c^{Mg})]-$$
$$\nabla\cdot[\rho(c_l^{Mg}-c^{Mg})(\boldsymbol{V}-\boldsymbol{V}_s)] \quad (8)$$

Liquid−particle interaction equation:

$$\boldsymbol{V}_s-\boldsymbol{V}_l=\frac{(1-g_s)}{18\mu_m}(\rho_s-\rho_l)d^2\boldsymbol{g} \quad (9)$$

The mixture dependent variables and mixture material properties in the conservation equations are defined as follows:

$\rho=g_l\rho_l+g_s\rho_s$, $c=f_lc_l+f_sc_s$, $\boldsymbol{V}=f_l\boldsymbol{V}_l+f_s\boldsymbol{V}_s$, $H=f_lH_l+f_sH_s$,

$c_{p,m}=f_lc_{p,l}+fc_{p,s}$, $k=g_lk_l+g_sk_s$, $H_s=c_{p,s}T$,

$H_l=c_{p,l}T+(c_{p,s}-c_{p,l})T_{sol}+L$ (10)

2.2 Thermodynamic relationships

Closure of the system of conservation equations requires thermodynamic relationships. In this work, the Gulliver−Scheil model (Eq. (11)) was used to calculate the solidification path, according to the phase diagrams, which were formulated as simple, approximate, analytical expressions [18,19,22]. This stand-alone microscopic module for the calculation of the solidification path of Al−Mg−Cu alloys in the Al rich corner of the phase diagram was solved simultaneously with macroscopic transport equations.

$$\begin{cases} c_l^i=c^i,\ f_s=0, & T>T_{Liq} \\ c^i=\int_0^{f_s}k^ic_l^i(f_s')\mathrm{d}f_s'+(1-f_s)c_l^i, & T=T_{Liq}(c_l^i), \\ \quad T_{Liq}\geq T>T_{Eut} & \\ c_l^i=c_{Eut}^i,\ f_s=1.0, & T\leq T_{Eut} \end{cases} \quad (11)$$

where the liquidus temperature T_{Liq} and the partition coefficient k_i were expressed as [23]

$$T_{Liq}=660-339.4c_l^{Cu}-538.5c_l^{Mg}-438.8c_l^{Cu}c_l^{Mg} \quad (12)$$

$$k^{Cu}=0.12,\quad k^{Mg}=0.32-0.52c_l^{Cu}+1.82c_l^{Mg} \quad (13)$$

The ternary Al alloy considered in this work (Al−4.5%Cu−1.5%Mg, mass fraction) has low content of Cu and Mg, so only the Al-rich corner of the system was modeled. It could be found that Eq. (12) for the projected liquidus surface was close to the results calculated by DU et al [15] with THERMO-CALC (as shown in Fig. 1).

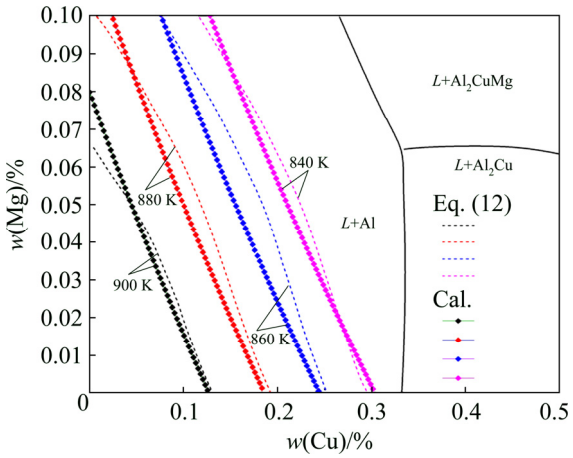

Fig. 1 Phase diagram for projected liquidus surface by Eq. (12) compared with result calculated by DU et al [15] with THERMO-CALC

2.3 Permeability model

The mushy zone was treated as a porous medium. The permeability was approximated by the well-known Carman−Kozeny relationship. The friction in the molten aluminum alloys was considered as a momentum source. The porosity was equal to the liquid fraction in the cell. In fully solidified regions, the porosity was equal to zero, which extinguished the velocities in these regions. The source item was calculated by following equations [24]:

$$S=\frac{\mu_l(1-f_l)^2\rho u}{K_0(f_l^3+\varepsilon)\rho_l} \quad (14)$$

$$K_0=\frac{\lambda_2^2}{180} \quad (15)$$

where μ_l is the liquid viscosity, f_l is the liquid fraction, K_0 is the permeability coefficient, ε is a small number (0.001) to prevent division by zero, ρ_l and ρ are the liquid density and the mixture density, respectively, u is the liquid velocity, and λ_2 is the secondary dendrite arm space. In this work, a permeability coefficient $K_0=2.0\times10^{-11}$ m^2 is used. This value is based on a dendrite arm spacing of 60 μm, which was measured by the experiment of DORWARD and BEERNTSEN [21].

3 Calculation program and model validation

3.1 Numerical solution procedures

The conservation equations were solved by computational fluid dynamics software FLUENT, which discretized all equations with the finite volume method. The scheme of pressure−velocity coupling was applied

with SIMPLE algorithm. The second-order upwind scheme was adopted to deal with the convection term of momentum and concentration equations. The first-order upwind scheme was selected for energy equation. Sources, permeability model and complex boundary conditions were hooked to FLUENT model by UDFs (user define functions). The mesh grid precision was 1 mm × 1 mm. For each time-step, 40 iterations were necessary, and 0.005 s for time step size was adopted to obtain sound convergence.

3.2 Thermophysical properties

The thermophysical parameters obtained from the Ref. [15,25], given in Table 1, were used in the calculation. The relationship of density of liquid phase, namely, $\rho_l=\rho_l(T,\ c_l)=\rho_0[1-\beta_T(T-T_0)-\beta_c(c-c_0)]$, was only applied into momentum equation. In addition, the values of specific heat and thermal conductivity were reduced to constant.

Table 1 Thermophysical properties and parameters

Parameter	Value
Liquid density, ρ_l/(kg·m^{-3})	2606
Solid density, ρ_s/(kg·m^{-3})	2750
Liquid specific heat, c_l/(J·kg^{-1}·K^{-1})	1054
Solid specific heat, , c_s/(J·kg^{-1}·K^{-1})	958
Liquid thermal conductivity, k_l/(W·m·K^{-1})	95.0
Solid thermal conductivity, k_s/(W·m·K^{-1})	180
Liquid diffusion coefficient, $D_l^{Cu/Mg}$/(m^2·s^{-1})	5.0×10^{-9}/ 2.0×10^{-8}
Liquid viscosity, μ_l/(kg·m^{-1}·s^{-1})	0.0013
Average solid viscosity, $\bar{\mu}_s$/(kg·m^{-1}·s^{-1})	$4.96\mu_l$
Solutal expansion coefficient, $\beta_l^{Cu/Mg}$/K^{-1}	−0.73/0.5
Thermal expansion coefficient, β_T/K^{-1}	1.17×10^{-4}
Melting point of Al, T_m/K	933.5
Eutectic temperature, T_{Eut}/K	780
Eutectic composition (mass fraction), $c_{Eut}^{Cu/Mg}$/%	44.8/17.2
Equilibrium partition coefficient, k_p (Cu)	0.12
Reference temperature, T_0/K	884
Reference concentration (mass fraction), c_0(K) (Cu/Mg)/%	4.5/1.5
Permeability constant, K_0/m^2	2.0×10^{-11}

3.3 Geometric model and boundary conditions

3.3.1 Geometric model and mesh

The 2D axisymmetric solution domain and mesh used in the calculation are shown in Fig. 2. The ingot with diameter of 400 mm and length of 950 mm was simulated. 50 mm in width was set for the inlet and hot-top, 100 mm in length for the water-cooled mold, and 950 mm for the water film. The mesh grid precision was 1 mm × 1 mm.

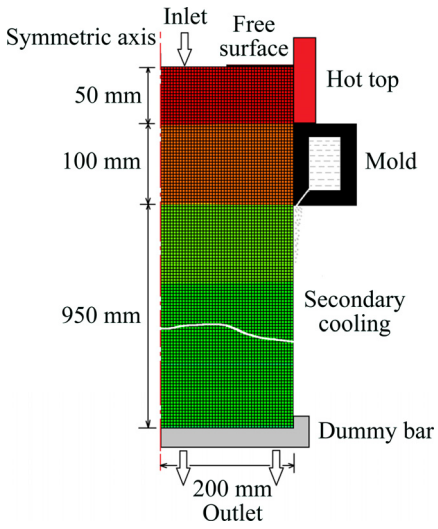

Fig. 2 Schematic diagram of direct chill casting and geometry mesh (mesh size of 1 mm × 1 mm)

3.3.2 Initial and boundary conditions

Initial conditions: the pouring temperature was 980 K, and the content of copper and magnesium were 0.045 and 0.015, respectively.

Boundary conditions: The inlet velocity was 254 mm/min, the outlet velocity was 63.5 mm/min, and free surface, hot top and symmetry axis were treated as the static adiabatic wall. For the mold-casting interface, the heat transfer coefficient h was treated as

$$h=h_{con}\times(1-f_s)+h_{air}\times f_s \tag{16}$$

where h_{con} is 1500 W/(m^2·K), and h_{air} is 150 W/(m^2·K).

In the secondary cooling region, the following Weckman−Niessen correlation [26] was used for heat transfer coefficient:

$$h_{Sec}(T)=(-167000+352(T-T_{water}))\cdot\left(\frac{Q_{water}}{P}\right)^{1/3}+20.8\left[\frac{(T-T_{saturation})^3}{T-T_{water}}\right] \tag{17}$$

where Q_{water} is the water flow rate with the value of 550 min^{-1}, P is the width of water film, $T_{saturation}$ is the saturation temperature of water, and T_{water} is the temperature of the cooling water with the value of 289.15 K.

No-slip boundary conditions were applied on the walls. The boundary conditions in the calculation were matched by the experiment as close as possible.

3.4 Validation of model

To validate this model in the prediction of macrosegregation, the numerical simulations were

applied into the numerical benchmark configuration proposed by BELLET et al [27] , which is usually used to evaluate the accuracy of the simulation results of the macrosegregation. The benchmark configuration is shown in Fig. 3(a). The ingot was contained in a rectangular mold with 0.1 m in width and 0.06 m in height. The mold was cooled symmetrically by both left and right sides. The top and bottom walls were adiabatic. Notably, only a half of the model was calculated, due to the symmetry of the geometry. The mesh size in the benchmark simulation case is also 1 mm × 1 mm.

The calculated results for Sn−10%Pb are compared with COMBEAU et al [28] (IJL group). It can be seen that the final stage of macrosegregation (Fig. 3(b)) is in accordance with the predicted results by IJL group (Fig. 3(c)). Figure 3(d) demonstrates that the liquid fraction reaches 0 earlier than 350 s, corresponding to slightly negative off average concentration at the end of solidification in sample point *E*. Moreover, the experimental and numerical simulation results on macrosegregation in benchmark (Sn−3%Pb) were compared with those reported in BOUSSAA et al [29], resulting in good agreement. Overall, our results above show sound validation of the model.

4 Simulation results and discussions

4.1 Calculation results for thermal field, liquid flow and macrosegregation of Al−Cu−Mg ingot

The contours of the predicted temperature distribution at different solidification times are shown in Fig. 4(a). When the molten aluminum alloy enters a cavity comprised of the water-cooled mold and a starter block, the solidified shell is formed. The shape of the molten pool is wide and steep in the early stages. With the progress of solidification, the steady state is approached and the temperature profile tends to be flattened. The temperature gradient near the mold and the water-cooled surface is higher than that in the other parts, due to the high heat transfer or high convection velocities.

The distribution of velocity pattern and the stream function are given in Figs. 4(b) and (c), respectively. The melt feeds into the mold through the inlet, and flows

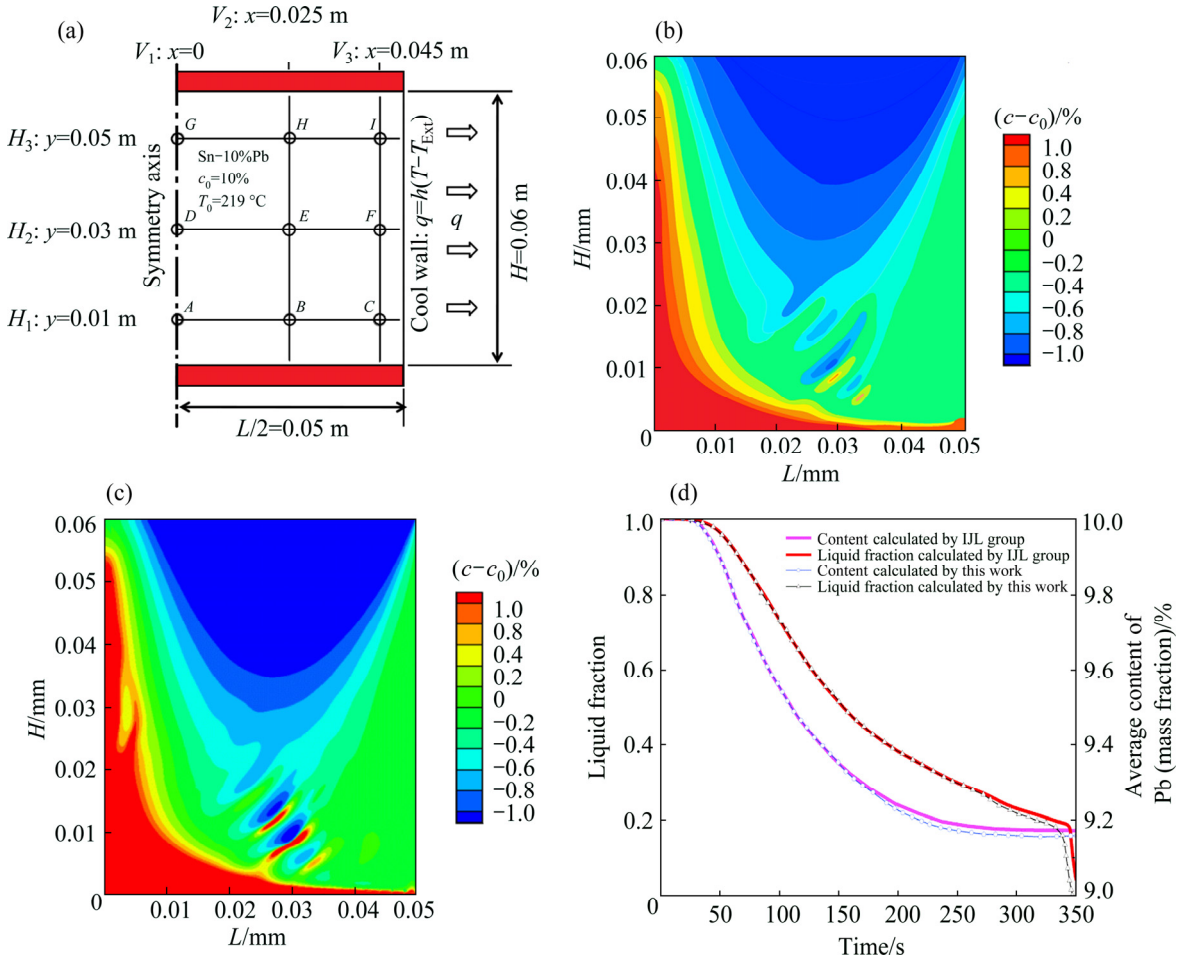

Fig. 3 Comparison of final segregation (Sn−10%Pb) calculated by this model with COMBEAU et al [28] (IJL group) in benchmark model: (a) Benchmark configuration; (b) Our work; (c) IJL; (d) Evolution of average content and liquid fraction in sample point *E* of Fig. 3(a)

toward the water-cooled mold along the liquid surface, due to the suction of solidification shrinkage. Subsequently, the melt descends down along the interface between the liquid and the mush zone toward the centerline in the low solid fraction region ($0<f_s<0.3$), owing to the driving force of thermal and solute buoyancy. In the high solid fraction region ($0.3<f_s<1.0$), the low permeability in the mushy zone blocks the driving force of buoyancy, making the velocity negligible. Subsequently, some flows deflect upward and form a clockwise recirculation. The ascending velocities decrease in the central regions, caused by the counteracting effect of thermal buoyancy and the incoming flow. Then, a stable region is formed in the center, as the floating dendrites settle down.

Due to the negative contribution of the third element of magnesium on thermosolutal convection, the magnitude of relative velocity decreases to some degree, compared with that in binary alloy. The melt is relatively stable along the radius away from the centerline (10 mm<r<100 mm). In the high solidification fraction region, the flow is governed by the shrinkage of solidification. The direction of this flow is parallel to the gradient of solidification fraction, as shown in Fig. 4(c).

The predicted copper segregation pattern is shown in Fig. 5(a), correspondingly, the concentration profile from the center to the surface of the ingot is given in Fig. 6. At the surfaces of the ingot, a positive segregation is obtained (about 3.8%) due to the solute-rich flow induced by shrinkage near the water cooling mold and exudation (the inverse segregation phenomenon). In adjacent to the surface, the clockwise recirculation induced by thermosolutal flow brings the solute-rich melt downwards the interface, creating a solute-lean subsurface region of negative segregation (about 4.0%). In the middle right section of the radius (100 mm<r<175 mm), about 2% positive relative segregation is formed owing to the thermosolutal convection and the rich-solute extruded by the accumulated dendrites in center region. In the ingot center, about 4% negative relative segregation is formed due to the solidification shrinkage and the accumulation of free floating dendrites. The positive segregation also forms at the bottom of the ingot, due to the solidification shrinkage. The segregation pattern for magnesium shows the similar trend in Fig. 5(b). In addition, the magnesium element to some extent alleviates the copper segregation in ternary alloy, compared with that in binary alloy [9].

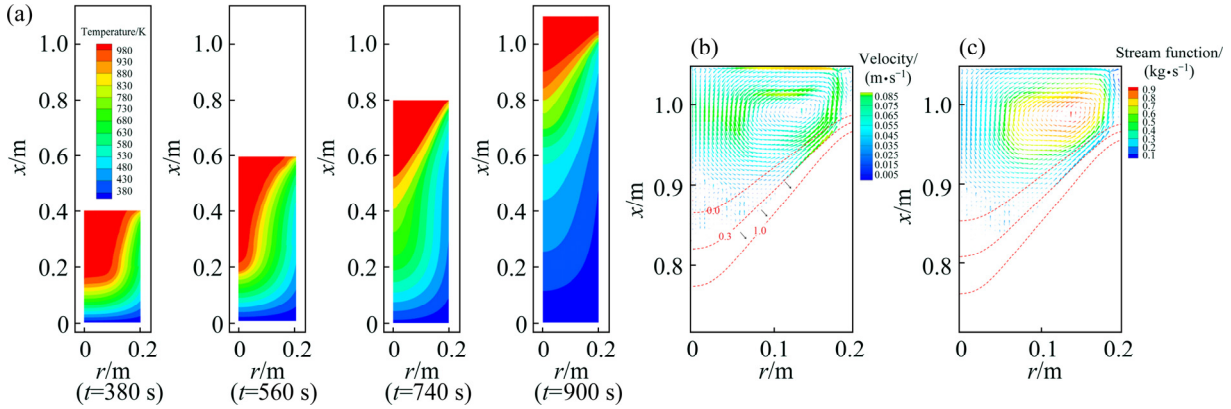

Fig. 4 Calculation results for Al−Cu−Mg ingot: (a) Evolution of temperature profiles; (b) Velocity pattern (v_l−v_s); (c) Stream function

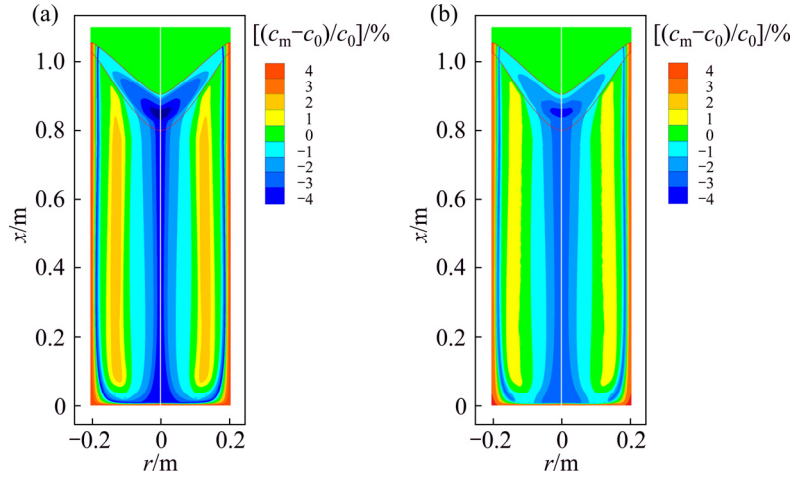

Fig. 5 Macrosegregation for Cu (a) and Mg (b) at 900 s

This could be mainly attributed to negative contribution to the solutal buoyancy by magnesium (opposite solute expansion coefficients for magnesium).

4.2 Comparison of macrosegregation between predicted results and experiments

The segregation depends on two opposing flows in the mushy zone and the sedimentation of floating grains. The thermosolutal buoyancy-induced flow transports the solute-rich liquid to the center and increases macrosegregation in the ingot center. On the opposite, contraction-driven flow transports solute-rich liquid to the outer surface and, hence, tends to alleviate the segregation in the central region of the ingot. The floating grains always have a tendency to create negative segregation where they accumulate. Final results depend on the factors dominating in the mushy zone.

DORWARD and BEERNTSEN [21] implemented a typical level feed, reservoir top DC semi-continuous system to cast 400 mm (diameter) ingot with a cast speed of 63.5 mm/min. The ingot slice was sawed at 800 mm. The concentrations were measured by 12.5 mm increments from surface to center. In our calculation, the simulation data were captured from the steady state.

Figure 6 shows that the simulation results are essentially in good agreement with the experimental results of DORWARD and BEERNTSEN [21]. In aluminum alloys, both copper and magnesium possess the partition coefficients less than 1. Therefore, it is not surprising that the overall segregation patterns of them are similar, i.e., negative segregation in the center and subsurface, and positive segregation in the middle section along the radius and surface. The extent of predicted segregation of magnesium is about 12% less than that of copper (Fig. 6). The reason for this is that the copper has the severer segregation tendency due to the lower partition coefficient. Although the qualitative agreement is found in comparison, the positive segregation region along the radius (100 mm<r<175 mm) is somewhat underestimated, attributed to three aspects. First, commercial aluminum alloys 2024 used by DORWARD and BEERNTSEN [21] have more than three alloying elements and impurities. Hence, there is to some degree grain refinement, and this effect can modify the resistance to flow through the solid network (mushy zone), decreasing the permeability in the mushy zone and lowering the coherency and rigidity temperatures. The lower permeability will hinder the shrinkage induced flow, narrow the rigid mushy zone, and prevent the penetration of convective flows into the rigid mushy zone. The lower coherency temperature means a wider slurry zone with more possibilities of convective flows and grain floating. Secondly, it is well known that the grain structure in large billets undergoes a columnar to equiaxed transition around the mid-radius, generated by fragmentation of the columnar dendrites. This produces a much larger slurry region and packing fraction than in simulation. Thirdly, in calculations, the packing fraction is set to be 0.3 as suggested in Ref. [10], which is not very accurate in this alloy. The lower composition at the centerline in experiments suggests that the actual packing fraction is set to be too low, because the degree of negative segregation increases with increasing packing fraction.

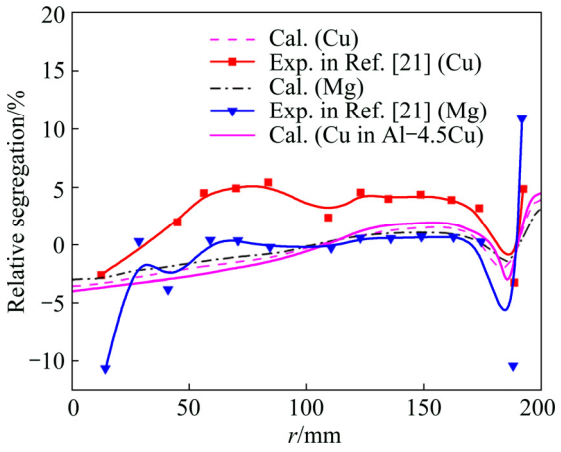

Fig. 6 Comparison of predicted results (relative segregation ($(c_m-c_0)/c_0$)) with experimental results

5 Conclusions

1) An extended continuum mixture model is used to predict macrosegregation in large size ingot of 2024 aluminum alloy, based on the numerical simulation of the mass, momentum, heat and solute transport during DC casting. The applicability of the model is validated by comparing calculation results with the benchmark of Sn−10%Pb (mass fraction).

2) The variations of temperature and velocity fields with time are obtained. The predicted results show that the positive segregation occurs in the radius middle section and surface of the ingot, and the negative segregation occurs in the center and subsurface. Moreover, the somewhat underestimated negative segregation is obtained in the radius middle section. The predicted results are quantitatively in accordance with the experimental observations.

3) The segregation in Al−Cu−Mg ternary alloy differs slightly from that in binary system Al−Cu even for Cu. The additional element of magnesium to some extent alleviates the copper segregation. The thermosolutal flow has the tendency to create the positive segregation, while the shrinkage flow exerts the opposite effect. The solute-lean floating grains have a tendency to create negative segregation where they accumulate. The model is firstly used to simulate the

macrosegregation in 2024 alloy accounting for the solidification shrinkage, thermosolutal convection and floating grain motion during DC casting.

Nomenclature

c	Content of alloying element (mass fraction)
f	Mass fraction
g	Volume fraction
$\boldsymbol{g}$	Gravitational acceleration (m/s^2)
H	Enthalpy (J/kg)
h	Convection heat transfer coefficient
K	Permeability (m^2)
k	Specific heat ($J\cdot kg^{-1}\cdot K^{-1}$)
L	Latent heat (J/kg)
t	Time (s)
T	Temperature (K)
$\boldsymbol{V}$	Velocity (m/s)
u	Axial velocity component (m/s)
v	Radial velocity component (m/s)
ρ	Density (kg/m^3)
i	Kind of alloying element

Subscripts

l	Liquid
s	solid
Eut	Eutectic
Liq	Liquidus
m	Mixture
con	Contact
Sec	Second

References

[1] ESKIN D G. Physical metallurgy of direct chill casting of aluminum alloys [M]. Boca Raton: CRC Press, 2008: 50−179.

[2] GRANDFIELD J F, ESKIN D G, BAINBRIDGE I. Direct-chill casting of light alloys [M]. Hoboken, New Jersey: John Wiley & Sons Inc, 2013: 144−169.

[3] ZUO Yu-bo, CUI Jian-zhong, MOU Dan, ZHU Qing-feng, WANG Xiang-jie, LI Lei. Effect of electromagnetic field on microstructure and macrosegregation of flat ingot of 2524 aluminium alloy [J]. Transactions of Nonferrous Metals Society of China, 2014, 24(7): 2408−2413.

[4] BENNON W D, INCROPERA F P. A continuum model for momentum, heat and species transport in binary solid−liquid phase change systems−I: Model formulation [J]. Int J Heat Mass Transfer, 1987, 30(10): 21−29.

[5] BECKERMANN C. A volume-averaged two-phase model for transport phenomena during solidification [J]. Metallurgical & Materials Transactions B, 1991, 22(3): 349−361.

[6] PICKERING E J. Macrosegregation in steel ingots: The applicability of modelling and characterisation techniques [J]. ISIJ International, 2013, 53(6): 935−949.

[7] AHMADEIN M, WU M, LUDWIG A. Analysis of macrosegregation formation and columnar-to-equiaxed transition during solidification of Al−4 wt.%Cu ingot using a 5-phase model [J]. Journal of Crystal Growth, 2015, 417: 65−74.

[8] REDDY A V, BECKERMANN N C. Modeling of macrosegregation due to thermosolutal convection and contraction-driven flow in direct chill continuous casting of an Al−Cu round ingot [J]. Metallurgical & Materials Transactions B, 1997, 28(3): 479−489.

[9] VREEMAN C J, KRANE M J M, INCROPERA F P. The effect of free-floating dendrites and convection on macrosegregation in direct chill cast aluminum alloys. Part I: Model development [J]. International Journal of Heat and Mass Transfer, 2000, 43(5): 667−686.

[10] VREEMAN C J, INCROPERA F P. The effect of free-floating dendrites and convection on macrosegregation in direct chill cast aluminum alloys. Part II: Predictions for Al−Cu and Al−Mg alloys [J]. International Journal of Heat and Mass Transfer, 2000, 43(5): 687−704.

[11] VREEMAN C J, SCHLOZ J D, KRANE M J M. Direct chill casting of aluminum alloys: Modeling and experiments on industrial scale ingots [J]. Transactions of the Asme Serie C Journal of Heat Transfer, 2002, 124(5): 947−952.

[12] KRANE M J M, INCROPERA F P, GASKELL D R. Solidification of ternary metal alloys−I. Model development [J]. International Journal of Heat & Mass Transfer, 1997, 40(16): 3827−3835.

[13] KRANE M J M, INCROPERA F P. Solidification of ternary metal alloys−II. Predictions of convective phenomena and solidification behavior in Pb−Sb−Sn alloys [J]. International Journal of Heat & Mass Transfer, 1997, 40(16): 3837−3847.

[14] KRANE M J M. Macrosegregation development during solidification of a multicomponent alloy with free-floating solid particles [J]. Applied Mathematical Modelling, 2004, 28(1): 95−107.

[15] DU Q, ESKIN D G, KATGERMAN L. Modeling macrosegregation during direct-chill casting of multicomponent aluminum alloys [J]. Metallurgical and Materials Transactions A, 2007, 38(1): 180−189.

[16] DORÉ X, COMBEAU H, RAPPAZ M. Modelling of microsegregation in ternary alloys application to the solidification of Al−Mg−Si [J]. Acta Materialia, 2000, 48(15): 3951−3962.

[17] VUŠANOVIĆ I. Macrosegregation of ternary Al−4.5wt%Cu−1.0wt%Mg alloy in horizontal direct chill casting: Implementation of non-equilibrium microsegregation model [J]. International Journal of Cast Metals Research, 2009, 22: 1−4.

[18] ELLINGSEN K, M'HAMDI M, TVEITO K, MORTENSEN D. Modelling of micro- and macrosegregation in multicomponent aluminium alloys accounting for secondary phase formation [J]. TMS Light Metals, 2014, 188(6): 861−866.

[19] ELLINGSEN K, MORTENSEN D, HAMDI M M. Modelling of micro- and macrosegregation for industrial multicomponent aluminium alloys [J]. Materials Science and Engineering, IOP Conference Series, 2015, 84(1): 12−58.

[20] NADELLA R, ESKIN D G, DU Q, KATGERMAN L. Macrosegregation in direct-chill casting of aluminium alloys [J]. Progress in Materials Science, 2008, 53(3): 421−480.

[21] DORWARD R C, BEERNTSEN D J. Effects of casting practice on macrosegregation and microstructure of 2024 alloy billet [J]. Light Metals, 1990: 825−830.

[22] ELLINGSEN K, DONS A L, M'HAMDI M, MO A, MORTENSEN D. New approach to quantifying solidification path in modelling of macrosegregation in multicomponent Al alloys [J]. International Journal of Cast Metals Research, 2009, 22(1−4): 220−223.

[23] VUŠANOVIĆ I, KRANE M J M. Microsegregation during solidification of Al−Cu−Mg alloys with varying composition [J]. International Communications in Heat & Mass Transfer, 2002, 29(8): 1037−1046.

[24] ZHANG Hai-tao, NAGAUMI H, ZUO Yu-bo, CUI Jian-zhong. Coupled modeling of electromagnetic field, fluid flow, heat transfer and solidification during low frequency electromagnetic casting of 7XXX aluminum alloys [J]. Materials Science and Engineering A, 2007, 448(1−2): 189−203.
[25] KRANE M, VUŠANOVIĆ I. Macrosegregation in horizontal direct chill casting of aluminium slabs [J]. Materials Science &Technology, 2009, 25(1): 102−107.
[26] WECKMAN D C, NIESSEN P. A numerical simulation of the DC continuous casting process including nucleate boiling heat transfer [J]. Metallurgical Transactions B, 1982, 13(4): 593−602.
[27] BELLET M, COMBEAU H, FAUTRELLE Y, GOBIN D, RADY M, ARQUIS E. Call for contributions to a numerical benchmark problem for 2D columnar solidification of binary alloys [J]. International Journal of Thermal Sciences, 2009, 48(11): 2013−2016.
[28] COMBEAU H, BELLET M, FAUTRELLE Y, GOBIN D, ARQUIS E, BUDENKOVA O. A numerical benchmark on the prediction of macrosegregation in binary alloys [C]//Supplemental Proceedings: Materials Fabrication, Properties, Characterization, and Modeling. John Wiley & Sons Inc, 2011: 755−762.
[29] BOUSSAA R, HACHANI L, BUDENKOVA O, BOTTON V, HENRY D, ZAIDAT K. Macrosegregations in Sn−3wt%Pb alloy solidification: Experimental and 3D numerical simulation investigations [J]. International Journal of Heat & Mass Transfer, 2016, 100: 680−690.

基于拓展连续模型的 2024 铝合金半连铸过程中的宏观偏析数值模拟

罗海军[1]，介万奇[1]，高志明[1]，郑永健[2]

1. 西北工业大学 凝固技术国家重点实验室，西安 710072；
2. Chair of Simulation and Modeling of Metallurgical Processes, Montan Universitaet Leoben, 8700 Leoben, Austria

摘　要：采用拓展连续模型预测大尺寸 2024 铝合金半连铸铸锭的 Cu 和 Mg 元素的偏析分布。该模型耦合宏观传输方程与近似相图的微观偏析模型来预测铸锭宏观偏析，并探讨传输机制对宏观偏析形成的影响。模拟结果表明，从铸锭中心到铸锭表面 Cu 元素和 Mg 元素具有相似的偏析分布，铸锭中心与紧邻铸锭表面的区域呈现负偏析分布，而铸锭表面和铸锭 1/2 半径处显示一定程度低估的正偏析分布, 并详细分析导致此结果的原因。此外，在三元铝合金中由于第三组元 Mg 元素的影响，Cu 元素的偏析相较铝铜二元合金中 Cu 元素的偏析要轻。计算结果表明预测值与文献实验结果基本一致。

关键词：半连铸；宏观偏析；数值模拟；连续模型；2024 铝合金

(Edited by Bing YANG)